

This is an Open Access document downloaded from ORCA, Cardiff University's institutional repository: <https://orca.cardiff.ac.uk/id/eprint/130516/>

This is the author's version of a work that was submitted to / accepted for publication.

Citation for final published version:

Charles, Bethan, Weller, Mark T., Rieger, Sebastian, Hatcher, Lauren E. , Henry, Paul F., Feldmann, Jochen, Wolverson, Daniel and Wilson, Chick C. 2020. Phase behavior and substitution limit of mixed cesium-formamidinium lead triiodide perovskites. *Chemistry of Materials* 32 (6) , pp. 2282-2291. [10.1021/acs.chemmater.9b04032](https://doi.org/10.1021/acs.chemmater.9b04032)

Publishers page: <http://dx.doi.org/10.1021/acs.chemmater.9b04032>

Please note:

Changes made as a result of publishing processes such as copy-editing, formatting and page numbers may not be reflected in this version. For the definitive version of this publication, please refer to the published source. You are advised to consult the publisher's version if you wish to cite this paper.

This version is being made available in accordance with publisher policies. See <http://orca.cf.ac.uk/policies.html> for usage policies. Copyright and moral rights for publications made available in ORCA are retained by the copyright holders.





# Phase Behavior and Substitution Limit of Mixed Cesium-Formamidinium Lead Tri-Iodide Perovskites.

Bethan Charles<sup>1</sup>, Mark T. Weller<sup>\*2</sup>, Sebastian Rieger<sup>3</sup>, Lauren E. Hatcher<sup>1</sup>, Paul F. Henry<sup>4,5</sup>, Jochen Feldmann<sup>3</sup>, Daniel Wolverson<sup>1</sup> and Chick C. Wilson<sup>1</sup>

<sup>1</sup>Centre for Sustainable Chemical Technologies, Departments of Chemistry and Physics, University of Bath, Bath BA2 7AY United Kingdom

<sup>2</sup>School of Chemistry, Cardiff University, Cardiff CF10 3AT, United Kingdom

<sup>3</sup>Chair for Photonics and Optoelectronics, Nano-Institute Munich, Department of Physics, Ludwig-Maximilians-Universität (LMU), Königinstr. 10, 80539 Munich, Germany

<sup>4</sup>ISIS Neutron and Muon Source, Rutherford Appleton Laboratory, Didcot, Oxfordshire OX11 0QX, United Kingdom

<sup>5</sup>Department of Chemistry and Chemical Engineering, Chalmers University of Technology, SE-412 96 Göteborg, Sweden

---

**ABSTRACT:** The mixed cation lead iodide perovskite photovoltaics show improved stability following site substitution of cesium ions ( $\text{Cs}^+$ ) onto the formamidinium cation sites ( $\text{FA}^+$ ) of  $(\text{CH}(\text{NH}_2)_2\text{PbI}_3$  (FAPbI<sub>3</sub>), and increased resistance to formation of the undesirable  $\delta$ -phase. The structural phase behavior of  $\text{Cs}_{0.1}\text{FA}_{0.9}\text{PbI}_3$  has been investigated by neutron powder diffraction (NPD), complemented by single crystal and power X-ray diffraction, and photoluminescence spectroscopy. The Cs substitution limit has been determined to be less than 15% and the cubic  $\alpha$ -phase  $\text{Cs}_{0.1}\text{FA}_{0.9}\text{PbI}_3$  is shown to be synthesizable in bulk and stable at 300 K. On cooling cubic  $\text{Cs}_{0.1}\text{FA}_{0.9}\text{PbI}_3$  a slow, second order cubic to tetragonal transition is observed close to 290 K, with variable temperature NPD indicating the presence of the tetragonal  $\beta$ -phase, adopting the space group  $P4/mbm$ , between 290 K and 180 K. An orthorhombic phase or twinned tetragonal phase is formed below 180 K and the temperature for the further transition to a disordered state is lowered to 125 K compared to that seen in phase pure  $\alpha$ -FAPbI<sub>3</sub> (140 K). These results demonstrate the importance of understanding the effect of cation site substitution on structure-property relationships in perovskite materials.

---

1. INTRODUCTION: FA site of the FAPbI<sub>3</sub> structure can significantly improve device lifetimes, enhancing the thermal and

The popularity of hybrid halide perovskites has skyrocketed moisture stability of thin films when compared to pure FAPbI<sub>3</sub> over recent years due to significant improvements to already<sup>15</sup>. Yi *et al.* attributed the enhanced stability provided by the Cs impressive photovoltaic (PV) device efficiencies<sup>1</sup>. A vast arraycation to the improved crystallization of the  $\alpha$ -phases, as cation of perovskite compositions have been explored, the mostmixing in the  $\alpha$ -phase is more energetically favorable than that effective taking on an  $\text{ABX}_3$  structure where the A, B and X-in the  $\delta$ -phase for the  $\text{CsPbI}_3$  and FAPbI<sub>3</sub> structure types<sup>16</sup>. sites are occupied with an organic cation, lead and a halideHowever, there is confusion concerning the structures of the anion respectively<sup>2</sup>. However, perovskite devices have beenmixed Cs-FA lead iodide perovskites, with contradictory plagued with stability problems<sup>3</sup>. One of the archetypical PVinformation on whether the composition  $\text{Cs}_{0.1}\text{FA}_{0.9}\text{PbI}_3$  adopts perovskites, formamidinium lead iodide  $(\text{CH}(\text{NH}_2)_2\text{PbI}_3$ ,a tetragonal or cubic structure at room temperature<sup>17-20</sup>, and FAPbI<sub>3</sub>), has been found to be too unstable for use inthe phase behavior of the mixed Cs-FA cation perovskite commercial devices, forming a PV-inactive yellow hexagonal  $\delta$ -remains poorly understood. It is crucial that the fundamental phase at room temperature and only stabilizing as the blackstructural properties of these mixed Cs-FA cation materials are cubic  $\alpha$ -phase above 60 °C<sup>4-7</sup>. In recent years cesium leadfully understood in order to appreciate PV device operation iodide ( $\text{CsPbI}_3$ ) has also been investigated, although in aacross different environments. similar fashion to FAPbI<sub>3</sub>,  $\text{CsPbI}_3$  transitions from the desirable The phase behavior as a function of temperature of the parent  $\alpha$ -perovskite phase to a yellow PV-inactive, non-perovskite  $\delta$ -material formamidinium lead iodide (FAPbI<sub>3</sub>) has been phase under ambient conditions<sup>8-10</sup>. described in previous work<sup>32</sup>. Results from neutron powder diffraction and synchrotron X-ray diffraction experiments are

In the drive to improve PV device efficiencies and lifetimes,consistent with the formation of two low temperature phases numerous studies have demonstrated that chemical siterelated to the room temperature cubic phase of  $\alpha$ -FAPbI<sub>3</sub>. The substitution at one or more of the perovskites' A, B or X sitesfirst transition to a primitive can improve the material's stability and PV performance<sup>11-14</sup>.tetragonal Incorporating small amounts of Cs at the

1 temperature at ~285 K and is associated with restricted  
2 motion of the FA<sup>+</sup> cations. On cooling below 140 K, a further  
3 phase transition occurs to  $\gamma$ -FAPbI<sub>3</sub> in which the FA<sup>+</sup> cation  
4 positions demonstrate a high level of disorder in a glassy state  
5 - though some elements of long-range ordering of the cations  
6 or tilting of the PbI<sub>6</sub> octahedra persists.

7 In this paper we present a detailed overview of the phase  
8 behavior of mixed Cs-FA lead iodide perovskites between 300  
9 and 100 K using neutron powder diffraction, complemented  
10 with X-ray diffraction (single crystal and powder) and  
11 variable temperature photoluminescence. Significant  
12 quantities of mixed cation perovskite powders were  
13 synthesized based on the method of Poglitsch and Weber<sup>22</sup>  
14 and single crystals of the same compositions were grown  
15 according to the method of Saidaminov *et al.*<sup>23, 24</sup>. It was  
16 found that no more 15% Cs could be incorporated into the  
17 FAPbI<sub>3</sub> structure through the synthetic methods used,  
18 therefore a single phase of the composition Cs<sub>0.1</sub>FA<sub>0.9</sub>PbI<sub>3</sub>  
19 was investigated in this work in detail. Inclusion of 10% Cs  
20 into methylammonium and formamidinium perovskites for  
21 use in PV devices is frequently reported in the literature due  
22 to the significantly improved PV performance; this serves as  
23 an additional incentive to focus on the Cs<sub>0.1</sub>FA<sub>0.9</sub>PbI<sub>3</sub>  
24 composition<sup>15, 16, 25</sup>. The quality and composition of the  
25 synthesized samples were checked through powder X-ray  
26 diffraction (PXRD), scanning electron microscopy (SEM)  
27 and energy dispersive X-ray spectroscopy (EDX).  
28 Differential scanning calorimetry (DSC) was initially used  
29 to check for potential phase transition temperatures.

## 30 2. MATERIALS AND METHODS:

### 31 2.1 Materials Synthesis:

32 Hydrogenous formamidinium iodide (FAI-H) was  
33 purchased from GreatCell Solar, all other reagents were  
34 purchased from Merck and solvents were purchased from Alfa  
35 Aesar (unless specified otherwise), with purities >99%.

36 *Cs<sub>0.1</sub>FA<sub>0.9</sub>PbI<sub>3</sub>-H powder.* Precipitation of the mixed cation  
37 perovskite Cs<sub>0.1</sub>FA<sub>0.9</sub>PbI<sub>3</sub> was based on the method by  
38 Poglitsch and Weber<sup>22</sup>. 0.0810 g (3.12×10<sup>-4</sup> moles) of  
39 cesium iodide (CsI), 0.4823 g (2.82×10<sup>-3</sup> moles) of  
40 formamidinium iodide (FAI-H) and 1.4367 g (3.12×10<sup>-3</sup>  
41 moles) of lead iodide (PbI<sub>2</sub>) were added to 3.12 ml of HI  
42 (+1.5 wt% H<sub>3</sub>PO<sub>4</sub>) in a three necked flask fitted with a  
43 condenser and nitrogen gas inlet, thereby forming a  
44 reaction mixture with the molar ratios Cs:FA:Pb of 0.1:0.9:  
45 1.0. The solution was heated to 100 °C under nitrogen and  
46 stirring, the stirring was then stopped, and the solution  
47 kept at 100 °C for 45 minutes before being cooled to 45 °C  
48 over 1 hour. The resulting powder was filtered, and oven  
49 dried at 100 °C overnight. See supplementary information  
50 S1 for details of reactant quantities used in the synthesis of  
51 Cs<sub>x</sub>FA<sub>1-x</sub>PbI<sub>3</sub> (x = 0.15, 0.2).

52 *Cs<sub>0.1</sub>FA<sub>0.9</sub>PbI<sub>3</sub>-H crystals.* Crystal growth by inverse  
53 solubility of the mixed cation perovskite Cs<sub>0.1</sub>FA<sub>0.9</sub>PbI<sub>3</sub> was  
54 prepared based on the method by Saidaminov *et al.*<sup>23, 24</sup>.  
55 0.0810 g (3.12×10<sup>-4</sup> moles) of CsI, 0.4823 g (2.82×10<sup>-3</sup> moles)  
56 of FAI and 1.4367 g (3.12×10<sup>-3</sup> moles) of PbI<sub>2</sub> were

dissolved at 80 °C in 3.46 ml of  $\gamma$ -butyrolactone (GBL). The  
57 solvent GBL had first been dried over calcium chloride  
58 (CaCl<sub>2</sub>). The solutions were heated to 110 °C at a rate of 10  
59 °C/hour, the growth of larger crystals could be achieved by  
60 decreasing the ramp rate. The temperature was increased to  
61 120 °C for a further hour before the resulting crystals were  
62 filtered from the remaining solution and oven dried at 100 °C  
63 overnight. The method was repeated to achieve the desired  
64 quantity of perovskite crystals. See supplementary  
65 information S1 for details of reactant quantities used in the  
66 synthesis of Cs<sub>x</sub>FA<sub>1-x</sub>PbI<sub>3</sub> (x = 0.15, 0.2).

67 *FAI-D powder.* Partial deuteration of the phases of  
68 interest was attempted with the aim of reducing the level  
69 of incoherent scattering, thereby increasing data quality  
70 through a higher signal-to-noise ratio in the neutron  
71 powder diffraction study. Part-deuterated FAI was  
72 obtained by dissolving hydrogenous FAI in a large excess  
73 of D<sub>2</sub>O under an argon atmosphere and stirring for 60  
74 minutes, the D<sub>2</sub>O was then evaporated and the sample  
75 dried under vacuum. The extent of deuteration was  
76 determined by the disappearance of the NH resonance in  
77 <sup>1</sup>H NMR spectrum. Only partial deuteration of the cation  
78 could be achieved resulting in the composition CH(ND<sub>2</sub>)<sub>2</sub>I.

79 *Cs<sub>0.1</sub>FA<sub>0.9</sub>PbI<sub>3</sub>-D powder.* With the aim of producing a multi-  
80 gram sample of part-deuterated Cs<sub>0.1</sub>FA<sub>0.9</sub>PbI<sub>3</sub>, 0.405  
81 g (1.559×10<sup>-3</sup> moles) of dried CsI, 2.412 g ((1.378×10<sup>-2</sup>  
82 moles) of FAI-D and 7.184 g (1.55×10<sup>-2</sup> moles) of dried  
83 PbI<sub>2</sub> were dissolved in 25.97 ml of dimethyl sulfoxide  
84 (DMSO-d<sub>6</sub>, from Merck 99.9% atom % D. The solution was  
85 drop cast onto preheated glass dishes at 150 °C on a hot  
86 plate in a dry box. As the solvent evaporated a black solid  
87 formed which was subsequently dried on the hotplate for a  
88 further 120 minutes. The sample was sealed under  
89 nitrogen and stored below 5 °C to reduce H-D exchange.

### 90 2.2 Characterization:

91 *Powder X-ray diffraction (PXRD)* data were collected on a  
92 Bruker Advance D8 diffractometer (Bragg-Brentano  
93 geometry) and a STOE STADI P (Debye-Scherrer  
94 geometry) using CuK $\alpha$  radiation ( $\lambda$  = 1.54060 Å). Indexing  
95 and peak fitting were carried out in GSAS-II<sup>26</sup> on  
96 Cs<sub>0.1</sub>FA<sub>0.9</sub>PbI<sub>3</sub> samples synthesized via inverse solubility  
97 (subsequently ground using a pestle and mortar) and the  
98 precipitation method.

99 *Single crystal X-ray diffraction (SXRD)* data were  
100 collected on a RIGAKU SuperNova dual tube Eos S2 CCD  
101 diffractometer using Mo ( $\lambda$  = 0.7107 Å) radiation. Suitable  
102 single crystals of Cs<sub>0.1</sub>FA<sub>0.9</sub>PbI<sub>3</sub> synthesized via inverse  
103 solubility were selected and measured at 300 K using an  
104 exposure of 10 s/frame, the sample was then cooled and  
105 measured at 175 K, 150 K and 120 K using an increased  
106 exposure of 20 s/frame. The structure was solved using  
107 the programs Olex2<sup>27</sup>, ShelXL<sup>28</sup> and PLATON<sup>29</sup>.

108 *Neutron powder diffraction (NPD)* was carried out on the  
109 POLARIS<sup>30</sup> instrument at the ISIS Neutron and Muon  
110 Source, Rutherford Appleton Laboratories. Approximately  
111 6 g of Cs<sub>0.1</sub>FA<sub>0.9</sub>PbI<sub>3</sub>-D was loaded into a 5 mm vanadium

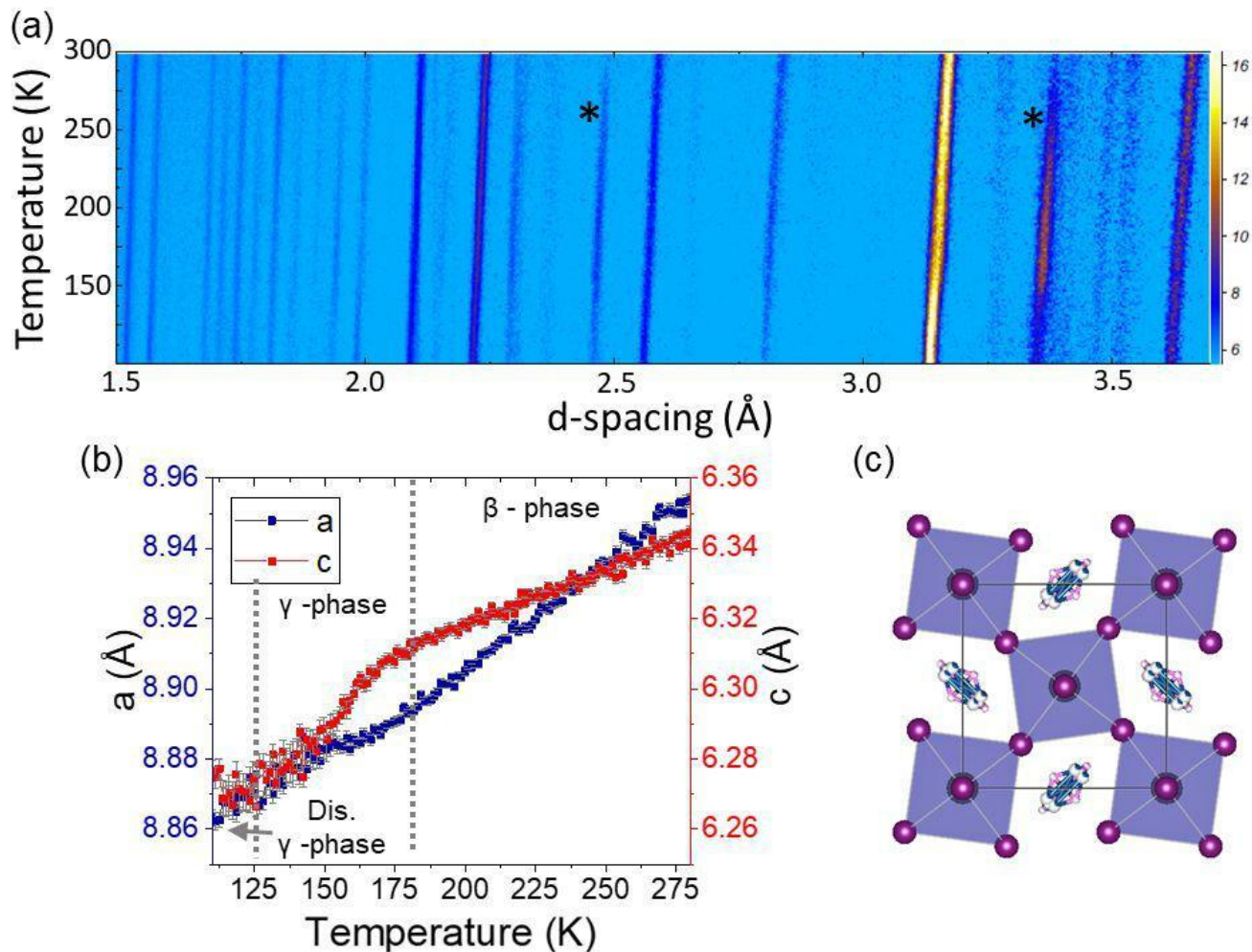


**Figure 1.** (a) Contour plot of neutron powder diffractograms on a  $\text{Cs}_{0.1}\text{FA}_{0.9}\text{PbI}_3$ -D sample stacked by temperature recorded on POLARIS at ISIS neutron and muon source: \* indicates prominent emergent peaks. (b) Sequential refinement of pseudo-tetragonal cell from 280 K to 110 K with transition temperatures marked by dashed grey lines. (c) Tetragonal model of the  $\beta$ -phase used in the sequential refinement. The model failed to fit data above 280 K coinciding with the gradual second order transition to the  $\alpha$ -phase.

sample can under argon and sealed using an indium O-ring. The sample was cooled to 100 K in the instrument cryofurnace and data were collected over 2 hours. The sample was subsequently heated at 1 K/min to 175 K, where a second 2-hour collection was recorded, before being cooled to 110 K at 1 K/min. Variable temperature diffraction data were recorded with an exposure time of 5 mins at a ramp rate of 0.2 K/min. A final 2-hour collection was measured at 300 K.

*Energy-dispersive X-ray (EDX)* spectroscopy was carried out using a Jeol JSM-6480LV SEM equipped with an Oxford INCA X-Act SDD X-ray detector using an accelerating voltage of 20 kV. The programs INCA and AZtec from Oxford Instruments were used to analyze chemical composition.

*Differential Scanning Calorimetry (DSC)* measurements were carried out on  $\text{Cs}_{0.1}\text{FA}_{0.9}\text{PbI}_3$  samples grown via inverse solubility and precipitation using a TA Instruments DSC Q20. Samples were cycled between 225 K and 420 K at a rate of 2 K/min.

*Steady state and transient photoluminescence (PL)* measurements were conducted using an in-house time-correlated single photon counter (TCSPC) set up. A single

crystal  $\text{Cs}_{0.1}\text{FA}_{0.9}\text{PbI}_3$  sample grown via inverse solubility was mounted onto a silica substrate using the polymer ZEONEX. The substrate was fixed in the CryoVac cryostat using Apezion grease and the cryostat pressure reduced to  $10^{-6}$  mbar using a TurboDrag pump. An NKT Photonics, SuperK Extreme, EXR-20 white light laser (WLL) together with a SuperK Select acousto-optic tunable filter (AOTF) were used to provide and tune the excitation signal and an Olympus SLCPFL 40x/0.55 long distance objective and CCD were used to collect the PL signal. Additional long pass, short pass and dichroic filters were used to block any remaining laser light, ensuring only the PL signal was recorded. The detector was calibrated using a xenon lamp.

### 3. RESULTS:

3.1 Cs Substitution Limit into  $\text{FAPbI}_3$  under these synthesis conditions. Samples of nominal compositions  $\text{Cs}_x\text{FA}_{1-x}\text{PbI}_3$  ( $0 < x < 0.2$ ,  $x = 0, 0.05, 0.10, 0.15$  and  $0.20$ ) were synthesized as single crystals through the inverse solubility method and as powder through the precipitation technique<sup>22-24</sup>. Samples of compositions up to  $x = 0.1$ ,  $\text{Cs}_{0.1}\text{FA}_{0.9}\text{PbI}_3$ , could be successfully synthesized as single-phase black powder and single crystals.

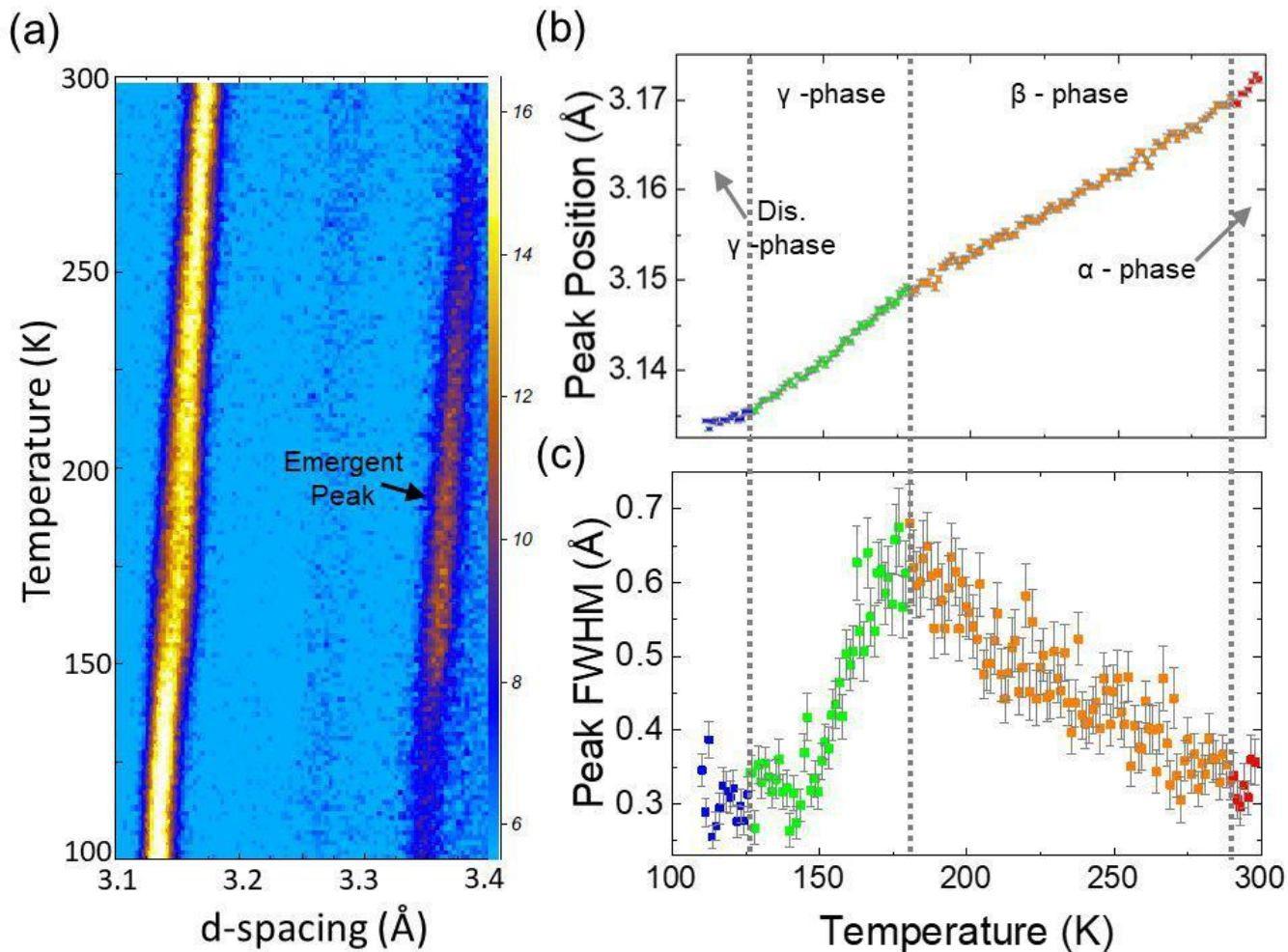


**Figure 2.** (a) Contour plot of neutron powder diffractograms on a  $\text{Cs}_{0.1}\text{FA}_{0.9}\text{PbI}_3$ -D sample stacked by temperature recorded on POLARIS at ISIS neutron and muon source in the range of 3.1 - 3.4 Å. (b) Resulting peak position of the sequential peak fit on the dominant peak centered at 3.15 Å. (c) FWHM as a function of temperature of the dominant peak. (a) and (c) are divided into the cubic (red), tetragonal (orange), orthorhombic (green) and low temperature (blue) phases.

PXRD was subsequently used to support Cs incorporation into the material, which was shown by a contraction of the unit cell to 6.346 Å compared with 6.362 Å measured for pure cubic  $\text{FAPbI}_3$ <sup>7</sup> (See supplementary information S2, S3 and S4 for PXRD, SEM, EDX Cs-maps and optical images).

$\text{Cs}_{0.15}\text{FA}_{0.85}\text{PbI}_3$  samples grown via the inverse solubility method in this work showed some additional peaks in PXRD data attributed to very small amounts of  $\delta$ - $\text{FAPbI}_3$  (see supplementary information for PXRD measurements). PXRD showed  $\text{Cs}_{0.1}\text{FA}_{0.9}\text{PbI}_3$  samples grown by inverse solubility were phase pure, whereas very small quantities (< 2%) of impurities were observed in the nominal  $\text{Cs}_{0.1}\text{FA}_{0.9}\text{PbI}_3$  powder samples synthesized through precipitation; these could be attributed to small amounts of both  $\delta$ - $\text{CsPbI}_3$  and  $\delta$ - $\text{FAPbI}_3$  possibly formed post-phase formation as shown in the supplementary information Figure S3). However, single crystal and powder samples synthesized with nominal compositions  $\text{Cs}_x\text{FA}_{1-x}\text{PbI}_3$  with  $x$

0.15 showed increasingly significant phase separation into black and yellow components, identified through PXRD as the  $\alpha$  and  $\delta$ -phases (Figure S2 in the supplementary information). Attempted SEM analysis of single crystals of

the nominal composition  $\text{Cs}_{0.2}\text{FA}_{0.8}\text{PbI}_3$  showed significant levels of  $\delta$ -phase needles on their surface, rendering accurate EDX compositional measurements highly unreliable. The  $\delta$ -phases identified in the PXRD measurements could be indexed to both the hexagonal  $\delta$ - $\text{FAPbI}_3$  and small quantities of the orthorhombic  $\delta$ - $\text{CsPbI}_3$ , agreeing with previous observations<sup>31</sup>.

Any analysis of the product compositions using PXRD and EDX should take due account of the limitations of these methods in determining accurate and precise compositions. PXRD compositional analysis of heavy element containing phases is likely to have errors of at least 2-3% and EDX measurements will have, at least, similar or larger error margins and be highly surface sensitive. Our results demonstrate a substitution limit of less than 15% Cs, but probably above 10%, into the  $\text{FAPbI}_3$  structure when synthesized through the inverse solubility method (see supplementary information for details regarding EDX measurements on these samples). Analysis of the single crystals using EDX suggested a preferred level of Cs inclusion near  $x = 0.12 \pm 0.02$ , i.e.  $\text{Cs}_{0.12}\text{FA}_{0.88}\text{PbI}_3$ . As the determined substitution limit was similar for both powder and crystal samples synthesized independently by the

1 precipitation and inverse solubility methods respectively,  
2 the composition with  $x$  slightly below the limit, i.e.  
3  $\text{Cs}_{0.1}\text{FA}_{0.9}\text{PbI}_3$ , was chosen for further investigation using  
4 NPD, SXRD and PL.

5 A limit of  $x < 0.15$  for  $\text{Cs}_x\text{FA}_{1-x}\text{PbI}_3$  is similar to that  
6 found in thin films of  $\text{Cs}_x\text{MA}_{1-x}\text{PbI}_3$  where MA is the cation  
7 methylammonium ( $\text{CH}_3\text{NH}_3^+$ )<sup>32</sup> frequently employed in  
8 photovoltaic perovskites. Using solid state NMR, Kubicki *et al.*  
9 determined a 15% limit of Cs incorporation into  $\text{FAPbI}_3$   
10 powder, observing the appearance of additional  $\delta$ - $\text{CsPbI}_3$   
11 peaks for  $x \geq 0.2$ <sup>31</sup>. On the other hand, Prasanna *et al.*  
12 reported 25% incorporation of Cs into thin films<sup>19</sup>. It is  
13 probable that 12% Cs is the thermodynamically preferred  
14 level of incorporation for mixed Cs-FA lead iodide  
15 perovskites grown via the inverse solubility method; this  
16 limit is likely to derive from the observation that  
17 crystallization is highly dependent on the ability to form a  
18 supersaturated solution before 110 °C, the temperature at  
19 which  $\text{FAPbI}_3$  crystallizes<sup>23,24</sup>.

20 3.2 Variable Temperature NPD and DSC. The phase  
21 behavior of  $\text{Cs}_{0.1}\text{FA}_{0.9}\text{PbI}_3$ -D was tracked using variable  
22 temperature NPD on the POLARIS instrument at ISIS  
23 neutron and muon source. A sample of  $\text{Cs}_{0.1}\text{FA}_{0.9}\text{PbI}_3$ -D was  
24 cooled to 100 K and subsequently heated in situ at a rate of  
25 0.2 K/min with data collected continuously and binned into 1  
26 K ranges between 100 K and 300 K. Data from the 90° bank  
27 were used due to the range in  $d$ -spacing, resolution and  
28 count-rate matching the requirements of the experiment.  
29 Patterns with  $d$ -spacing ranging between 1.5 Å  
30 – 3.69 Å are displayed as stacked plots in Figure 1a.

31 A continuous shift in peak positions can be seen in  
32 Figure 1a, representing decreasing unit cell volume with  
33 decreasing temperature. Figure 1a also shows the  
34 emergence of additional peaks between 290 K and 180 K  
35 indicating decreasing symmetry from 298K. The additional  
36 peaks represent the emergence of the tetragonal  $\beta$ -phase.  
37 Formation of a tetragonal phase with distinct  $a$  and  $c$   
38 lattice parameters occurs below 290 K in agreement with  
39 DSC data, which shows a phase transition centered at 290  
40 K (see supplementary information S6, Figure S4). The  
41 width of the DSC peak centered at 290 K indicates a very  
42 slow transition occurring between 310 K and 273K. This  
43 slow transition reflects the glassy nature of hybrid halide  
44 perovskites, with the central organic cation known to  
45 exhibit slow, glass-like reorientational dynamics leading to  
46 disordered phases<sup>33-36</sup>. The width of this phase transition  
47 could be a source of the confusion as to the room  
48 temperature structure of  $\text{Cs}_{0.1}\text{FA}_{0.9}\text{PbI}_3$ <sup>17-20</sup>.

49 Below 180 K in the NPD data, the intensity of some of  
50 the emergent peaks decreases (see the (211) hkl values  
51 reflection near 3.35 Å in Figure 2a) corresponding to the  
52 transformation to an orthorhombic  $\gamma$ -phase and ongoing  
53 cooling of this phase. The origin of the loss in intensity in  
54 reflections such as the (211) is likely to be associated with  
55 the convergence of the reduced  $a$  and  $c$  lattice parameters  
56 (see Figure 1) in this temperature regime; the intensity of  
57 such reflections will be dependent on differences in the  
58 degree of tilting of the  $\text{PbI}_6$  octahedra along the  $a$  and  $c$   
59 lattice directions and as these two converge the reflection  
60 intensity is reduced. However, full analysis would require  
61 a detailed modeling of the iodide positions over this

temperature range which is beyond the modeling than can  
be justified with the data resolution and quality available.

Trends in the shift and intensity of peaks were investigated  
using sequential refinement in GSAS II<sup>26</sup>. A pseudo-cubic  
model was first used from the refinement of NPD data at 300  
K; however, it became apparent that a tetragonal model  
would better describe the structural behavior over the vast  
majority of the temperature range investigated. The  $\beta$ -phase  
tetragonal model obtained from a long collection at 200 K and  
based on that developed by Weber *et al.* for  $\text{FAPbI}_3$  and was  
used<sup>21</sup>. The tetragonal space group  $P4/mbm$  was used, and  
the part deuterated FA cation was modelled as a rigid CH-  
NHD molecule. In this model the carbon atom of the  
formamidinium cation is assigned to a site with coordinates  
(0.5,  $y$ , 0.5) with  $y \sim 0.5$  and refinement showed that  $y=0.5$   
within the extracted error. The  $\text{Cs}^+$  cation will also occupy a  
site very close to (0.5, 0.5, 0.5) and Cs and C have similar  
neutron scattering lengths (5.42 fm and 6.64 fm). This means  
that, with the low level of Cs, developing a structural model  
which had a distinct Cs site with a site occupancy of 0.1 was  
not justified

– indeed attempts to do this and refine a model with both  
Cs and FA cations result in an unstable, non-converging  
refinement. Therefore, the model used in the analysis used  
a central carbon site at (0.5, $y$ ,0.5) with  $y \sim 0.5$  to represent  
both the 90% formamidinium carbon and 10% Cs; note  
that this modeled the profile peak intensities well and did  
not, of course, affect the extracted information such as  
crystal system or lattice parameters.

This model was refined against shorter NPD collections  
at higher temperatures but failed to provide a suitable fit  
above 280 K, corresponding with the slow second order  
transition to the cubic  $\alpha$ -phase. The model was  
subsequently refined again against the 280 K NPD pattern,  
which was used as a starting point to the sequential  
refinement covering all data sets collected below this  
temperature. Lattice parameters extracted as a function of  
temperature from the sequential refinement are shown in  
Figure 1b.

The evolution (positions and halfwidth) of the dominant  
peak centered at 3.15 Å (Figure 2a) was also analyzed using  
sequential peak fitting in GSAS II. Changes in the position of  
this peak position and its FWHM correspond to the phase  
transition points suggested by the earlier sequential  
refinement of a pseudo-tetragonal structure. These changes in  
gradient of the peak shift (Figure 2b) are observed at 290 K,  
180 K and 125 K corresponding with the cubic, tetragonal,  
orthorhombic and disordered low temperature phases  
respectively. Peak broadening can be used as an indicator for  
peak splitting corresponding to changing symmetry.  
Extracted values of the dominant peak full width at half  
maximum (FWHM) as a function of temperature (Figure 2c)  
indicate clear broadening below 290 K which can be assigned  
to the formation of distinct peaks indicative to the tetragonal  
structure. An abrupt change in FWHM shift is observed at the  
orthorhombic transition by 180 K. This is an artifact of  
modeling the true orthorhombic structure with a tetragonal  
unit cell in which the  $a$  and  $c$  lattice parameters (see Figure 1)  
are rapidly converging. The reflection at 3.15 Å is the (200)  
reflection and equivalents in the room temperature cubic  
phase. This splits into the

(200) and (002) reflections for the tetragonal phase and further for the orthorhombic description. The convergence in the positions of the (200), (020) and (002) reflections and equivalents as the  $c$  lattice parameter decreases rapidly on cooling from 180 K. Example profile fits obtained during the SEQGSAS refinements, at 112 K, 145 K, 225 K and 255 K are included in the supplementary information, S9.

3.3 Cubic  $\alpha$ -Cs<sub>0.1</sub>FA<sub>0.9</sub>PbI<sub>3</sub>, > 290 K. The structure of Cs<sub>0.1</sub>FA<sub>0.9</sub>PbI<sub>3</sub> above 290 K was investigated via NPD, PXRD and SXRD.

Fully hydrogenated, phase pure Cs<sub>0.1</sub>FA<sub>0.9</sub>PbI<sub>3</sub> samples synthesized by the inverse solubility method, and ground using a pestle and mortar, were investigated using PXRD at RT. PXRD patterns indexed best to the cubic  $Pm\bar{3}m$  space group and revealed a shift in the (100) peak in comparison to  $\alpha$ -FAPbI<sub>3</sub> due to an expected contraction of the lattice on Cs incorporation<sup>18</sup>. Figure 3b shows the indexed PXRD pattern obtained at 298 K from a STOE STADI P diffractometer. PXRD was also used to check the quality of part deuterated samples synthesized by the drop casting method for NPD measurements. Impurity peaks were identified and indexed to small quantities (< 2%) of  $\delta$ -CsPbI<sub>3</sub> and  $\delta$ -FAPbI<sub>3</sub> (see supplementary information, S4).

NPD data obtained at 300 K from a 2-hour collection on POLARIS at the ISIS neutron and muon source was fully analyzed using the GSAS II software. Lattice parameters from the indexed PXRD data were used as a starting point for further refinement.

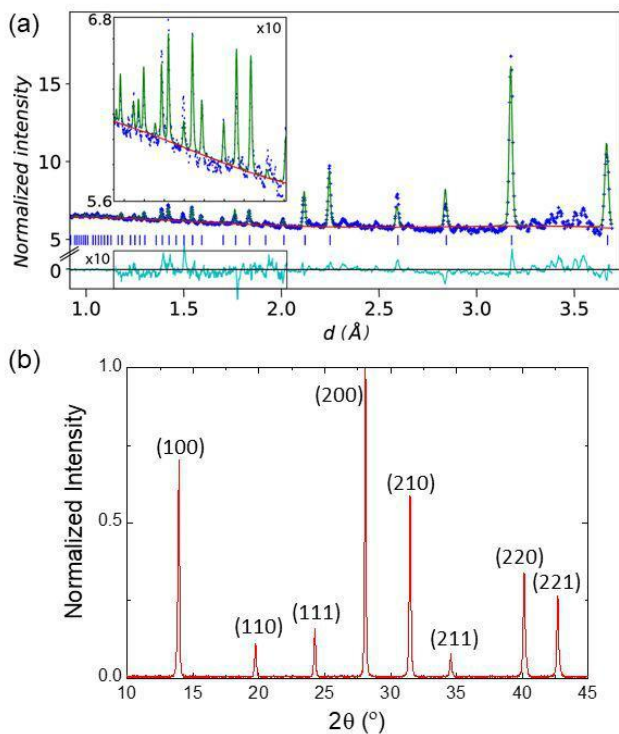


**Figure 3.** (a) Rietveld fit (red) on NPD data (blue) collected on POLARIS at 300 K and (insets - boxed) enlarged areas, x10, of fit between  $d$ -spacing 1.2 – 2 Å. Data were refined to space group  $Pm\bar{3}m$  with lattice parameter  $a = 6.34562(24)$  Å,  $wR = 1.69\%$ . The difference between the observed and calculated values is

shown in light blue. Regions between 2.32 Å – 2.44 Å and 3.44 Å – 3.56 Å could be assigned to  $\delta$ -phase impurities. (b) PXRD data indexed to a cubic cell in  $Pm\bar{3}m$ .

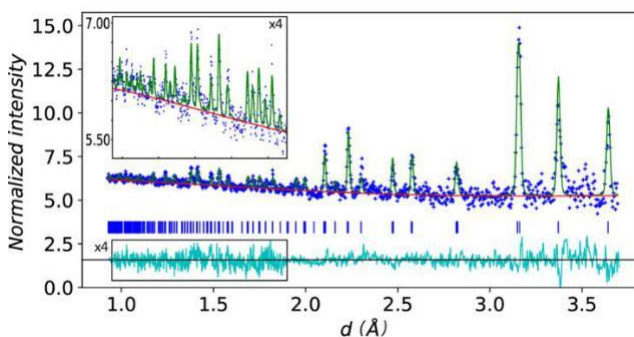


**Figure 4.** Rietveld fit on NPD data collected on POLARIS at 200 K and (insets - boxed) enlarged areas, x4, of fit between  $d$ -spacing 0.9 – 1.9 Å. Data were refined to space group  $P4/m\bar{3}m$ ,  $a = 8.9084(8)$  Å  $c = 6.3224(8)$  Å,  $wR = 2.90\%$ . Regions between 2.32 Å – 2.44 Å and 3.44 Å – 3.56 Å could be assigned to  $\delta$ -phase impurities.

Initially the structural description of the FA cation in FAPbI<sub>3</sub> at 298 K was used as a model<sup>7</sup>, atomic positions were used as published and only lattice and instrumental parameters were varied at first. The planar part-deuterated FA cation was modelled to a rigid H-C-N-HD molecule, with initial isotropic atomic displacement parameters (ADPs) of 0.5 Å<sup>2</sup> set. As performed by Weller *et al.*<sup>7</sup> for FAPbI<sub>3</sub>, the C-H atoms were assigned a site occupancy of 0.16, while the single N-HD group was modelled with an occupancy of 0.0833, together describing the 12 orientations of the planar FA cation within the cuboctahedral void. As described for the tetragonal phase analysis the Cs<sup>+</sup> cation was not modeled independently but represented by the carbon atom of a fully occupied FA site. This initial refinement produced a good fit of the data, with a  $wR$  of 1.92%. Subsequent refinement of the Pb and I ADPs produced a slightly improved fit, with  $wR$  of 1.89%. The ADPs of the C, N, H and D making up the rigid FA cation were constrained to be equal, and when refined, the  $wR$  improved to 1.72% leading to a value of 0.244(6) Å<sup>2</sup>. The high thermal parameter values indicate significant rotational motion of the FA cation at 300 K. The position of the whole cation was then refined, producing the cubic structural model detailed in the supplementary information, in space group  $Pm\bar{3}m$  with lattice parameter  $a$

$= 6.34562(24)$  Å,  $wR$  1.69%. Further crystallographic information is given in the supplementary information S5 and associated CIF. Despite some earlier studies suggesting Cs<sub>0.1</sub>FA<sub>0.9</sub>PbI<sub>3</sub> adopts a tetragonal structure in ambient conditions<sup>19</sup>, we do not observe peak splitting in this high-resolution data that would indicate tetragonal symmetry.

Single crystals of  $\alpha$ -Cs<sub>0.1</sub>FA<sub>0.9</sub>PbI<sub>3</sub> grown via inverse solubility were selected to obtain a structural model at 300 K using SXRD data. Two methods were used. Firstly, the established structure for  $\alpha$ -FAPbI<sub>3</sub> was used as a model, accounting for the low scattering and tumbling of the FA cation by modelling the A-site as a single atom with a large ADP. Secondly, the structure was solved in the low symmetry space group  $P1$  before the validation software PLATON was used to determine a more suitable space



group. In both cases the best solution fit to  $Pm3m$  with lattice parameter  $a = 6.2780(3)$  Å. Generated (pseudo-) precession figures, supplementary information S10, also confirmed the cubic symmetry at 300K.

Large anisotropic ADPs associated with on axis iodine atom in the SXRD refinement suggest significant oscillation of the  $PbI_6$  octahedra. An attempt was made to model the observed spread of electron density to locked octahedral tilts as predicted from *ab initio* methods by Gosh *et al.*<sup>18</sup>; however, any ordered tilting of the  $PbI_6$  octahedra could not be modeled. We therefore resolved that the time averaged structure of  $Cs_{0.1}FA_{0.9}PbI_3$  is cubic at 300 K, although the local structure may contain pseudo-tetragonal domains due to tilted octahedra switching rapidly between preferred directions. Pair distribution function analysis has shown the  $Pb^{2+}$  cation to be displaced at ambient temperatures in  $FAPbI_3$  resulting in concerted displacement of the iodide anions<sup>37</sup> and these displacements potentially contribute to the extracted large ADPs modeled in our SXRD measurements on  $Cs_{0.1}FA_{0.9}PbI_3$ . However we do not have the resolution in our NPD data to model such local order.

Further studies probing the local structure of these complex materials would be valuable including high-resolution XRD measurements investigating displacements of the B and X-site anions and cations would be useful.

**3.4 Tetragonal Phase,  $\beta$ -  $Cs_{0.1}FA_{0.9}PbI_3$ , 290 K – 180 K.** Variable temperature NPD was used to investigate the tetragonal  $\beta$ -phase that was found to exist between 290 K and 180 K; the transition to this phase is characterized by the appearance of the tetragonal unit cell (211) reflection as seen centered at  $d = 3.37$  Å in Figure 4. Rietveld fits were performed on NPD data collected at 200 K and based on the model developed by Weber *et al.* for pure  $FAPbI_3$ <sup>21</sup>. The part-deuterated FA cation was modeled as a rigid H-C-N-HD molecule with an occupancy of 0.5 for the C atom and 0.25 for the N, H and D, representing the restricted motion of the cation in the tetragonal phase<sup>21</sup>. ADPs for the Pb and I were then refined, producing lower values than those obtained in the cubic phase, suggesting reduced motion of the  $PbI_6$  octahedra. The thermal parameters for C, N, H and D of the FA cation were constrained to be equal, refining to give  $0.190(9)$  Å<sup>2</sup>. The position of the rigid cation was then refined to give the tetragonal structural model described in the supplementary information and associated CIF, S5. The refinement converged to a cell in the space group  $P4/mbm$ , lattice parameters  $a = 8.9084(8)$  Å and  $c = 6.3224(8)$  Å,  $wR = 2.90\%$ . The tetragonal model fits the data well from 180 K to 280 K, above this temperature refinements failed as the material gradually transitioned to the cubic  $\alpha$ -phase. Additional example profile fits obtained during these SEQGSAS refinements, at 225 K and 255K are included in the supplementary information, S9.

**3.5 Y-  $Cs_{0.1}FA_{0.9}PbI_3$  phase 180 K – 125 K.** The structure of the parent phase  $FAPbI_3$  can be modelled using a tetragonal unit cell for all temperatures below 180 K<sup>21, 38, 39</sup>. Analysis of the SXD data obtained from  $Cs_{0.1}FA_{0.9}PbI_3$  at 175 K and 150 K showed the issues normally found for perovskitic phases of this type which undergo a phase transition to a lower cell symmetry on cooling. As has been observed for  $FAPbI_3$ , it seems that  $Cs_{0.1}FA_{0.9}PbI_3$  forms crystallographic twins when cooled through phase transitions, leading to

large residuals and challenges identifying the absolute structure<sup>21</sup>. Thus SXRD data obtained at 175 K could be indexed to either crystallographic twins in the tetragonal space group  $P4/mbm$ , or orthorhombic  $Pnma$ . Refined lattice parameters for the orthorhombic description were  $a = 8.8217(16)$  Å,  $b = 12.5912(17)$  Å and  $c = 8.7242(16)$  Å. Example profile fits obtained during the SEQGSAS refinements, at 112 K and 145 K, are included in the supplementary information, S9.

For SXD data collected at 150 K the best fits using an orthorhombic space group;  $Pnma$  at 150 K where lattice parameters extracted were  $a = 8.8192(12)$  Å,  $b = 12.5777(13)$  Å and  $c = 8.6274(13)$  Å; however a crystallographically twinned tetragonal model in  $P4/mbm$  could not be fully discounted. Note that in both these structural models that  $c/\sqrt{2} \times a$  is less than 1.01 supporting the observation that these models could not be distinguished from tetragonal in the neutron powder diffraction study. In addition, these data support the observation of a rapid decrease in the c lattice parameter in this temperature range – as seen in the NPD data, Figure 1b.

**3.6 Low Temperature Phase, < 125 K.** SXRD data collected at 120 K converged to the space group  $Pnma$  with lattice parameters  $a = 8.8215(11)$  Å,  $b = 12.5815(13)$  Å,  $c = 8.6091(13)$  Å. However, unlike the higher temperature data, additional weak reflections were observed at 120 K which could be attributed to the formation of a disordered state. The emergence of disorder at low temperature agrees with previous findings for  $FAPbI_3$  in which residual entropy causes the freezing of FA cation rotation and locking of the  $PbI_6$  octahedra in a glass-like state<sup>21, 33-37, 39</sup>. As with the parent phase  $FAPbI_3$  some elements of long range ordering associated with the cations or, more likely, the tilting of the  $PbI_6$  octahedra persist below 120 K - this generates the observed additional diffraction intensity seen for  $Cs_{0.1}FA_{0.9}PbI_3$ .

**3.7 Variable Temperature PL.** A single crystal of  $Cs_{0.1}FA_{0.9}PbI_3$  synthesized via the inverse solubility method was mounted in a cryostat and illuminated with an excitation wavelength of 630 nm while the temperature was varied from 290 K to 25 K. Each PL spectrum was fitted with a single Gaussian function subsequently used to analyze the peak PL positions and FWHM (Figure 5a, b, c). It should be noted that spectra taken at 290 K and 275 K were fitted using a second Gaussian term to account for photon reabsorption effects in the 1 mm thick crystal<sup>40</sup>. These reabsorption peaks were not included in the peak PL position and FWHM analysis.

Peak positions extracted from Gaussian fits of the PL were plotted as a function of temperature (Figure 5b) revealing a red shift with decreasing temperature familiar to these family of hybrid halide perovskites<sup>41, 42</sup>. This shift has been attributed to stabilization of the valence band maximum due to a combination of thermal expansion effects and electron-phonon interactions<sup>43</sup>. Below 125 K a blue shift in peak position is observed. Interestingly the blue shift at low temperatures correlates with the transition to the disordered state as revealed through XRD and NPD measurements presented in this work. A change in PL shift at low temperature has been previously linked to disorder

in MAPbX<sub>3</sub> hybrid halide perovskites, attributed to band filling effects induced

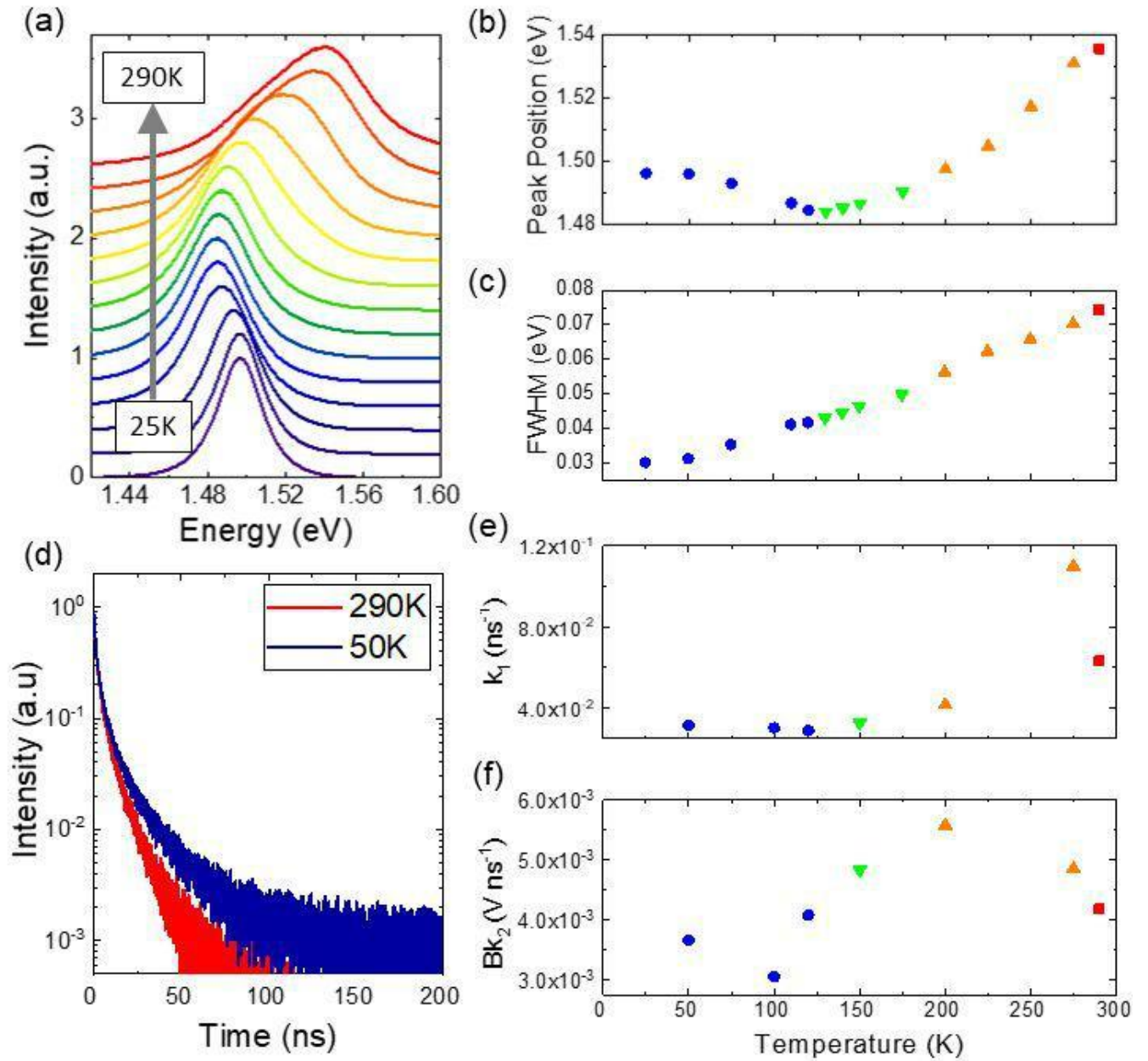


**Figure 5.** (a) Variable temperature steady state PL on a single crystal of Cs<sub>0.1</sub>FA<sub>0.9</sub>PbI<sub>3</sub>. (b) Peak positions and (c) FWHM of the Gaussian fits to PL as a function of temperature. (d) PL decay measured at 290 K and 50 K. (e) Extracted monomolecular recombination rate constants ( $k_1$ ) and (f) effective bimolecular rate constant ( $Bk_2$ ) from fits to variable temperature PL decay. Points are colored according to the cubic  $\alpha$ -phase (red square), tetragonal  $\beta$ -phase (orange triangles), orthorhombic  $\gamma$ -phase (green inverted triangles) and disordered low temperature phase (blue circles).

by a difference in band gap between domains of ordered and disordered cation orientations<sup>41</sup>.

The temperature dependence of the PL FWHM ( $\Gamma(T)$ ) can be expressed in terms of the below<sup>42,43</sup>:

$$\Gamma(T) = \Gamma_0 + Y_{LO} \exp\left(-\frac{E_{LO}}{k_B T}\right)$$

where  $T$  is temperature,  $k_B$  is the Boltzmann constant,  $\Gamma_0$  is the temperature independent homogeneous broadening term  $Y_{LO}$  is the charge carrier longitudinal-optical (LO) phonon coupling strength and  $E_{LO}$  is the energy for the LO phonon. The resulting FWHM of the Gaussian fits to the steady state PL could be modelled to Equation 1 (blue dashed line in Figure 5c), from which the extracted values for  $\Gamma_0$ ,  $Y_{LO}$  and  $E_{LO}$  were  $29 \pm 1$  meV,  $30 \pm 4$  meV and  $13 \pm 1$  meV respectively. There is possible grouping of the FWHM data according to phase in Figure 5c; however, the

discontinuities are small and proved difficult to model separately. Transient luminescence spectra for  $\text{Cs}_{0.1}\text{FA}_{0.9}\text{PbI}_3$  were measured at seven distinct temperatures between 290 K and 50 K inclusive (Figure 5d). The resulting spectra were modelled according to the charge-carrier recombination rate equation <sup>44</sup>:

$$-\frac{dn}{dt} = k_1 n + k_2 n^2 + k_3 n^3 \quad (2)$$

where  $n$  is the photogenerated carrier density and  $k_i$  is the recombination rate. Each term represents a charge carrier annihilation process following excitation, (1) being monomolecular recombination, (2) bimolecular recombination and (3) three body Auger recombination. Previous studies have shown first and second order recombination mechanisms to dominate in hybrid perovskites at moderate intensities, therefore Auger recombination was neglected <sup>45</sup>.

Values of  $k_1$ , determined from fitting PL decay with equation 2, are shown in Figure 5e. The monomolecular term is predominately determined by first order Shockley-Reed recombination in hybrid halide perovskites, therefore the value of  $k_1$  is dictated by trap-assisted recombination <sup>44</sup>. In general, the  $k_1$  decreases with decreasing temperature; however, a significant increase is seen between 290 – 275 K. This was potentially due to domains of cubic and tetragonal phases appearing over the phase transition and acting as recombination centers. Below the 125 K transition into the disordered structure the monomolecular recombination rate increases, possibly due to disordered domains acting as recombination centers <sup>41, 44</sup>.

Effective values of the bimolecular rate constant were measured as  $Bk_2$  <sup>46</sup>, where  $B$  is a proportionality constant as described in the supplementary information, S7. The values of  $Bk_2$  (Figure 5f) generally increase with decreasing temperature, until the transition to the low temperature disordered phase around 125 K. The reversal in trends observed for PL peak position,  $k_1$  and  $Bk_2$  below the 125 K transition clearly indicate the disordered nature of the FA cations and  $\text{PbI}_6$  orientations at low temperature affect the optoelectronic properties of the material. It is speculated that the presence of disordered domains act as recombination centers, so increasing the monomolecular and bimolecular recombination rates <sup>44</sup>.

#### 4. DISCUSSION:

The results of the investigation into the phase behavior of bulk  $\text{Cs}_x\text{FA}_{1-x}\text{PbI}_3$  are combined with those found for phase pure  $\alpha$ -FAPbI<sub>3</sub> and  $\alpha$ -CsPbI<sub>3</sub> to produce the phase diagram in Figure 6 <sup>10, 21</sup>. Cs and FA cation mixing is more energetically favorable in the  $\alpha$ -phase than  $\delta$ -phase <sup>16</sup>, leading to the preferred formation of cubic  $\alpha$ - $\text{Cs}_{0.1}\text{FA}_{0.9}\text{PbI}_3$  through synthesis by inverse solubility and precipitation from acid. Mixed Cs-FA crystals and powders remained stable in the black  $\alpha$ -phase in air at 20% humidity over one month. PXRD measurements on  $\text{Cs}_{0.1}\text{FA}_{0.9}\text{PbI}_3$  powders used in powder diffraction experiments showed negligible degradation or phase separation to  $\delta$ -FAPbI<sub>3</sub> and  $\delta$ -FAPbI<sub>3</sub> over 28 days (see supplementary information for PXRD measurements, S8). It was observed that after six months that partial phase separation had occurred in the mixed Cs-FA samples forming small regions of yellow  $\delta$  and black  $\alpha$  -

phase. This stability is much improved on that of  $\alpha$ -FAPbI<sub>3</sub>, which quickly transforms to  $\delta$ -FAPbI<sub>3</sub> on exposure to the atmosphere <sup>7</sup>. Lee *et al.* attributed the improved stability of  $\text{Cs}_x\text{FA}_{1-x}\text{PbI}_3$  to stronger interactions between the FA cations and I anions due to a contraction of the unit cell <sup>47</sup>.

A consequence of the improved stability of the mixed Cs-FA lead iodide perovskite is that the desirable black  $\alpha$ -phase

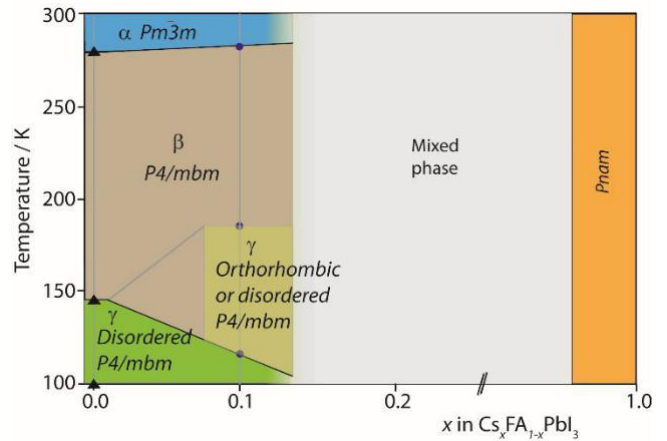


**Figure 6.** Schematic phase diagram for  $\text{Cs}_x\text{FA}_{1-x}\text{PbI}_3$  solid samples with estimated phase transition positions. Space groups and transition temperatures as found in this work (blue circles) from variable temperature NPD data on  $\text{Cs}_{0.1}\text{FA}_{0.9}\text{PbI}_3$  are compared with that found by Weber *et al.* <sup>21</sup> for FAPbI<sub>3</sub> (black triangles) and Sutton *et al.* <sup>10</sup> for CsPbI<sub>3</sub>.

becomes more accessible under ambient conditions. Numerous studies have shown the tetragonal ( $\beta$ ) to cubic ( $\alpha$ ) transition in quench cooled samples of  $\alpha$ -FAPbI<sub>3</sub> to occur at 285 K <sup>21, 38, 39</sup>. However, this transition is rarely observed as formation of the hexagonal  $\delta$ -FAPbI<sub>3</sub> phase is energetically favored at room temperature <sup>7</sup>. The variable temperature NPD data presented in this paper shows the tetragonal ( $\beta$ ) to cubic ( $\alpha$ ) transition temperature only slightly affected by the addition of 10% Cs into the FAPbI<sub>3</sub> structure, determined as 290 K for  $\text{Cs}_{0.1}\text{FA}_{0.9}\text{PbI}_3$  in this work.

There has been confusion whether  $\text{Cs}_{0.1}\text{FA}_{0.9}\text{PbI}_3$  adopts a cubic or tetragonal structure at room temperature <sup>18-20</sup>. Variable NPD data of  $\text{Cs}_{0.1}\text{FA}_{0.9}\text{PbI}_3$  suggested a slow, second-order transformation from the cubic  $\alpha$ -phase to a tetragonal phase centered close to 290 K. The proximity of the cubic-tetragonal transition to room temperature, in combination to the dynamic nature of the  $\text{PbI}_6$  octahedra, is likely to be a key factor as to why these differences in the reported room temperature structure of  $\text{Cs}_{0.1}\text{FA}_{0.9}\text{PbI}_3$  occur in the literature.

*Ab initio* studies have shown that addition of the smaller Cs cation into the FAPbI<sub>3</sub> structure results in a contraction of the cuboctahedral voids formed by the corner sharing  $\text{PbI}_6$  octahedra, resulting in geometric strain of the lead iodide framework, and leading to stronger hydrogen bonding between the amine groups of the FA cation and iodide <sup>18</sup>. These effects lead to the suppressed motion of the FA cation, and locked tilting of the  $\text{PbI}_6$  octahedra at lower temperatures <sup>17, 18</sup>, inducing the possible formation of an

1 additional orthorhombic  $\gamma$ -phase as seen in the variable  
2 temperature SXRD; the formation of an orthorhombic phase  
3 would also be consistent with the changes observed in the  
4 NPD data between 170 and  $\sim$ 125 K. As well as the appearance  
5 of this extra orthorhombic phase, the addition of Cs lowers  
6 the transition to a low temperature disordered state from 140  
7 K observed in pure FAPbI<sub>3</sub>, to 125 K as  
8 suggested by NPD, SXRD and PL for Cs<sub>0.1</sub>FA<sub>0.9</sub>PbI<sub>3</sub> in this  
9 work. Therefore, in addition to increasing resistance to  $\delta$ -  
10 phase formation, incorporating Cs into the FAPbI<sub>3</sub>  
11 structure has important effects resulting in the desirable  
12 cubic  $\alpha$ -phase being accessible at room temperature, the  
13 stabilization of an orthorhombic phase below  $\sim$ 180 K and  
14 lowering of the transition temperature to the disordered  
15 state below 125 K.

## 16 5. CONCLUSIONS:

17 The phase behavior of formamidinium lead iodide partially  
18 substituted with cesium (Cs<sub>x</sub>FA<sub>1-x</sub>PbI<sub>3</sub>,  $0 \leq x \leq 0.2$ ) has been  
19 investigated. PXRD data showed contraction in the lattice  
20 parameter when compared to pure FAPbI<sub>3</sub> indicating  
21 successful Cs incorporation for  $x < 0.15$ , and EDX  
22 measurements suggested the preferential formation of the  
23 composition Cs<sub>0.12</sub>FA<sub>0.88</sub>PbI<sub>3</sub> in high quality crystals  
24 synthesized by inverse solubility methods. From variable  
25 temperature NPD it was determined that inclusion of Cs  
26 results in formation of the desirable cubic  $\alpha$ -phase of  
27 Cs<sub>0.1</sub>FA<sub>0.9</sub>PbI<sub>3</sub> that exists at room temperature. Moreover,  
28 the formation of an orthorhombic phase is inferred on  
29 cooling below 180 K, and disorder attributed to residual  
30 entropy of FA cation orientation appeared only on cooling  
31 below 125 K. Our extensive study provides important  
32 insights into the intrinsic behavior of mixed cation  
33 perovskites commonly used in photovoltaics.

## 34 ASSOCIATED CONTENT

35 Supporting Information. Additional synthetic details, energy  
36 dispersive X-ray spectroscopy (EDX), differential scanning  
37 calorimetry, additional structural models and  
38 photoluminescence modelling.

## 39 AUTHOR INFORMATION

### 40 Corresponding Author

41 \* E-mail: [wellerml@cardiff.ac.uk](mailto:wellerml@cardiff.ac.uk)

### 42 Author Contributions

43 The manuscript was written through contributions of all  
44 authors. All authors have given approval to the final version of  
45 the manuscript. B.C. undertook sample synthesis. L.E.H., B.C.  
46 and C.C.W the X-ray diffraction experiments and analysis. B.C.,  
47 M.T.W and P.F.H. the neutron diffraction experiments and  
48 analysis. B.C., S.R., J.F. and D.W. performed the  
49 photoluminescence experiments and analysis.

### 50 Funding Sources

51 This work was supported by the Engineering and Physical  
52 Sciences Research Council EP/L016354/1, and the Bavarian

53 State Ministry of Science, Research, and Arts for funding  
54 through the grant Solar Technologies go Hybrid (SolTech) and  
55 the Deutsche Forschungsgemeinschaft (DFG, German  
56 Research Foundation) under Germany's Excellence Strategy –  
57 EXC 2089/1-390776260. We would also like to thank STFC  
58 for funding access to ISIS and the award of beamtime under  
59 proposal RB181080448.

## 60 Notes

The authors declare no competing financial interest.

## 61 ACKNOWLEDGMENT

62 Thank you to James Tellam of the ISIS deuteration facility for  
63 synthesis of the deuterated FAI, as well as Philip Fletcher,  
64 Maya Singer Hobbs, Christopher Daniel Scott and Alexander  
65 Richter for additional help with material synthesis and  
66 characterization. We also thank Jon Skelton and Dibya Ghosh  
67 for insightful discussions. We thank local research clusters  
68 and centers (such as CeNS) for providing communicative  
69 networking structures.

## 70 ABBREVIATIONS

71 MA, methylammonium; FA, formamidinium; PXRD, powder X-  
72 ray diffraction; SXRD, single crystal X-ray diffraction; NPD,  
73 neutron powder diffraction; PL, photoluminescence

## 74 REFERENCES

- 75 (1) Green, M. A.; Hishkawa, Y.; Dunlop, E.D.; Levi, D. H.; Hohl-  
76 Eblinger, J.; Yoshita, M.; Ho-Baillie, A.W.Y. Solar cell efficiency  
77 tables (Version 53). *Progress in PV*, 2019, 27 (1), 3-12
- 78 (2) Gratzel, M. The light and shade of perovskite solar cells.  
79 *Nat. Mater.*, 2014, 13 (9), 838-842
- 80 (3) Ashgar, M.I.; Zhang, J.; Wang, H.; Lund, P.D. Device stability  
81 of perovskite solar cells – A review. *Ren. Sus. Energy Rev.*, 2017,  
82 77, 131-146
- 83 (4) Zhao, L.; Kerner, R. A.; Xiao, Z.; Lin, Y. L.; Lee, K. M.;  
84 Schwartz, J.; Rand, B. P. Redox Chemistry Dominates the  
85 Degradation and Decomposition of Metal Halide Perovskite  
86 Optoelectronic Devices. *ACS Energy Lett.* 2016, 1 (3), 595–602
- 87 (5) Nagabhushana, G. P.; Shivaramaiah, R.; Navrotsky, A. Direct  
88 Calorimetric Verification of Thermodynamic Instability of Lead  
89 Halide Hybrid Perovskites. *Proc. Natl. Acad. Sci. U. S. A.* 2016, 113  
90 (28), 7717–7721.
- 91 (6) Stoumpos, C. C.; Malliakas, C. D.; Kanatzidis, M. G.  
92 Semiconducting Tin and Lead Iodide Perovskites with Organic  
93 Cations: Phase Transitions, High Mobilities, and near-Infrared  
94 Photoluminescent Properties. *Inorg. Chem.* 2013, 52 (15),  
95 9019–9038.
- 96 (7) Weller, M. T.; Weber, O. J.; Frost, J. M.; Walsh, A. Cubic  
97 Perovskite Structure of Black Formamidinium Lead Iodide,  $\alpha$ -  
98 [HC(NH<sub>2</sub>)<sub>2</sub>]PbI<sub>3</sub>, at 298 K. *J. Phys. Chem. Lett.* 2015, 6, 3209–3212.
- 99 (8) Eperon, G. E.; Paternò, G. M.; Sutton, R. J.; Zampetti, A.;  
100 Haghighirad, A. A.; Cacialli, F.; Snaith, H. J. Inorganic Caesium Lead  
101 Iodide Perovskite Solar Cells. *J. Mater. Chem. A.* 2015, 3 (39),  
102 19688– 19695.
- 103 (9) Sutton, R. J.; Eperon, G. E.; Miranda, L.; Parrot, E. S.; Kamino,  
104 B. A.; Patel, J. B.; Horantner, M. T.; Johnston, M. B.; Haghighirad, A.  
105 A.; Moore, D. T.; Snaith, H. J. Bandgap-tunable cesium lead halide  
106 perovskites with high thermal stability for efficient solar cells.  
107 *Adv. Energy Mater.*, 2016, 6 (8), 1502458
- 108 (10) Sutton, R. J.; Filip, M. R.; Haghighirad, A. A.; Sakai, N.; Wenger,  
109 B.; Giustino, F.; Snaith, H.J. Cubic or orthorhombic? Revealing the  
110 crystal structure of metastable black-phase CsPbI<sub>3</sub> by theory and  
111 experiment. *ACS Energy Lett.*, 2018, 3(8), 1787-1794
- 112 (11) Charles, B.; Dillon, J.; Weber, O. J.; Islam, M. S.; Weller, M. T.  
113 Understanding the stability of mixed A-cation lead iodide  
114 perovskites. *J. Mater. Chem. A.*, 2017, 5 (43), 22495-22499

- (12) Weber, O. J.; Charles, B.; Weller, M.T.; Phase behavior and composition in the formamidinium-methylammonium hybrid lead iodide perovskite solid solution. *J. Mat. Chem. A*, 2016, 4 (40), 15375-15382
- (13) Klug, M. T.; Osherov, A.; Haghighirad, A. A.; Stranks, S. D.; Brown, P. R.; Bai, S.; Wang, J. T-W.; Dang, X.; Bulovic, V.; Snaith H. J.; Belcher, A. M. Tailoring metal halide perovskites through metal substitution: influence on photovoltaic and material properties. *Energy Environ. Sci.*, 2017, 10 (1), 236-246
- (14) Matsui, T.; Seo, J-Y.; Saliba, M.; Zakeeruddin, A. M.; Gratzel, M. Room-temperature formation of highly crystalline multication perovskites for efficient, low-cost solar cells. *Adv. Mater.*, 2017, 29(15), 1606258
- (15) Syzgantseva, O.A.; Saliba, M.; Gratzel, M.; Rothlisberger, U. Stabilization of the perovskite phase of formamidinium lead triiodide by methylammonium, Cs, and/or Rb doping. *J. Phys. Chem. Lett.*, 2017, 8(6), 1191-1196
- (16) Yi, C.; Luo, J.; Meloni, S.; Boziki, A.; Ashari-Astani, N.; Gratzel, C.; Zakeeruddin, S. M.; Rothlisberger, U.; Gratzel, M. Entropic stabilization of mixed A-cation ABX<sub>3</sub> metal halide perovskites for high performance perovskite solar cells. *Energy Environ. Sci.*, 2016, 9 (2), 656
- (17) Gosh, D.; Atkins, P.W.; Islam, M. S.; Walker A. B.; Eames, C. Good vibrations: locking of octahedral tilting in mixed-cation iodide perovskites for solar cells. *ACS Energy Lett.*, 2017, 2 (10), 2424-2429
- (18) Gosh, D.; Smith, A. R.; Walker, A. B.; Islam, M. S. Mixed A-cation perovskites for solar cells: atomic-scale insights into structural distortion, hydrogen bonding, and electronic properties. *Chem. Mater.*, 2018, 30 (15), 5194-5204
- (19) Prasanna, R.; Gold-Parker, A.; Leijtens, T.; Conings, B.; Babayigit, A.; Boyen, H-G.; Toney M. F.; McGehee, M. D. Band gap tuning via lattice contraction and octahedral tilting in perovskite materials for photovoltaics. *J. Am. Chem. Soc.*, 2017, 139 (32), 11117-11124
- (20) Prathapani, S.; Bhargava, P.; Mallick, S. Electronic band structure and carrier concentration of formamidinium-cesium mixed cation lead mixed halide hybrid perovskites. *Appl. Phys. Lett.*, 2018, 112 (9), 092104
- (21) Weber, O. J.; Ghosh, D.; Gaines, S.; Henry, P. F.; Walker, A. B.; Islam M. S.; Weller, M. T. Phase behavior and polymorphism of formamidinium lead iodide. *Chem. Mater.*, 2018, 30 (11), 3768-3778
- (22) Poglitsch, A.; Weber, D. Dynamic disorder in methylammoniumtrihalogenoplumbates (II) observed by millimeter-wave spectroscopy. *J. Chem. Phys.*, 1987, 87 (11), 6373
- (23) Saidaminov, M. I.; Abdelhady, A. L.; Murali, B.; Alarousu, E.; Burlakov, V. M.; Peng, W.; Dursun, I.; Wang, L.; He, Y.; Maculan, G.; Goriely, A.; Wu, T.; Mohammed O. F.; Bakr, O. M. High-quality bulk hybrid perovskite single crystals within minutes by inverse temperature crystallization. *Nat. Comm.*, 2015, 6, 7586
- (24) Saidaminov, M. I.; Abdelhady, A. L.; Maculan, G.; Bakr, O. M. Retrograde solubility of formamidinium and methylammonium lead halide perovskites enabling rapid single crystal growth. *Chem. Comm.*, 2015, 51 (100), 17658-17661
- (25) Saliba, M.; Matsui, T.; Seo, J-Y.; Domanski, K. Correa-Baena, J-P.; Nazeeruddin, M. K.; Zakeeruddin S. M.; Tress, W.; Abate, A.; Hagfeldt, A.; Gratzel, M. Cesium-containing triple cation perovskite solar cells: Improved stability, reproducibility and high efficiency. *Energy Environ. Sci.*, 2016, 9, 6, 1989-1997
- (26) Toby, B. H.; Von Dreele, R. B. GSAS-II: the genesis of a modern open-source all-purpose crystallography software package. *J. Applied Crystallography*, 2013, 46 (2), 544-549.
- (27) Dolomanov, O.V.; Bourhis, L.J.; Gildea, R.J.; Howard, J.A.K.; Puschmann, H. OLEX2: A complete structure solution, refinement and analysis program. *J. Appl. Cryst.*, 2009, 42, 339-341
- (28) Sheldrick, G. M. Crystal Structure Refinement with SHELXL. *Acta Cryst.*, 2015, c71, 3-8
- (29) Speck, A. L. Structure validation in chemical crystallography, 2009, D65, 148-155
- (30) Smith, R. I.; Hull, S.; Tucker, M. G.; Playford, H. Y.; McPhail, D. J.; Waller, S. P.; Norberg, S. T. The Upgraded Polaris Powder Diffractometer at the ISIS neutron source. *Rev. Sci. Instrum.*, 2019, 90, 115101
- (31) Kubicki, D. J.; Prochowicz, D.; Hofstetter, A.; Zakeeruddin, S. M.; Grätzel, M.; Emsley, L. Phase segregation in Cs-, Rb- and K-doped mixed-cation (MA)<sub>x</sub>(FA)<sub>1-x</sub>PbI<sub>3</sub> hybrid perovskites from solid-state NMR. *JACS*, 2017, 139 (40), 14173-14180
- (32) Niemann, R. G.; Gouda, L.; Hu, J.; Tirosh, S.; Gottesman, R.; Cameron, P. J.; Zaban, A. Cs+ incorporation into CH<sub>3</sub>NH<sub>3</sub>PbI<sub>3</sub> perovskite: substitution limit and stability enhancement. *J. Mater. Chem. A*, 2016, 4 (45), 17819-17827
- (33) Fabini, D. H.; Siaw, T. A.; Stoumpos, C. C.; Laurita, G.; Olds, D.; Page, K.; Hu, J. G.; Kanatzidis, M. G.; Han, S.; Seshadri, R. Universal Dynamics of Molecular Reorientation in Hybrid Lead Iodide Perovskites. *J. Am. Chem. Soc.* 2017, 139 (46), 16875-16884.
- (34) Mozur, E. M.; Maughan, A. E.; Cheng, Y.; Huq, A.; Jalarvo, N.; Daemen, L. L.; Neilson, J. R. Orientational Glass Formation in Substituted Hybrid Perovskites. *Chem. Mater.* 2017, 29 (23), 10168-10177.
- (35) Govinda, S.; Kore, B. P.; Swain, D.; Hossain, A.; De, C.; Guru Row, T. N.; Sarma, D. D. Critical Comparison of FAPbX<sub>3</sub> and MAPbX<sub>3</sub> (X = Br and Cl): How Do They Differ? *J. Phys. Chem. C* 2018, 122 (25), 13758-13766.
- (36) Even, J.; Carignano, M.; Katan, C. Molecular Disorder and Translation/Rotation Coupling in the Plastic Crystal Phase of Hybrid Perovskites. *Nanoscale* 2016, 8 (12), 6222-6236.
- (37) Laurita, G.; Fabini, D. H.; Stoumpos, C. C.; Kanatzidis, M. G.; Seshadri, R. Chemical Tuning of Dynamic Cation Off-Centering in the Cubic Phases of Hybrid Tin and Lead Halide Perovskites. *Chem. Sci.* 2017, 8(8), 5628-5635
- (38) Fabini, D. H.; Stoumpos, C. C.; Laurita, G.; Kaltzoglou, A.; Kontos, A. G.; Falaras, P.; Kanatzidis, M. G.; Seshadri, R. Reentrant Structural and Optical Properties and Large Positive Thermal Expansion in Perovskite Formamidinium Lead Iodide. *Angew. Chem., Int. Ed.* 2016, 55 (49), 15392-15396.
- (39) Chen, T.; Chen, W.-L.; Foley, B. J.; Lee, J.; Ruff, J. P. C.; Ko, J.; Y. P.; Brown, C. M.; Harriger, L. W.; Zhang, D.; Park, C.; Yoon, M.; Chang, Y.-M.; Choi, J. J.; Lee, S.-H. Origin of Long Lifetime of Band-Edge Charge Carriers in Organic-inorganic Lead Iodide Perovskites. *Proc. Natl. Acad. Sci. U. S. A.* 2017, 114, 7519-752
- (40) Wenger, B.; Nayak, P. K.; Kesava, S. V.; Noel, N. K.; Snaith, H. J. Consolidation of the photoelectric properties of CH<sub>3</sub>NH<sub>3</sub>PbBr<sub>3</sub> perovskite single crystals. *Nat. Comm.*, 2017, 8, 590
- (41) M. I. Dar, G. Jacopin, S. Meloni, A. Mattoni, N. Arora, A. Boziki, S. M. Zakeeruddin, U. Rothlisberger, M. Grätzel, Origin of unusual bandgap shift and dual emission in organic-inorganic lead halide perovskites, *Science Adv.*, 2016, 2, 10
- (42) Wright, A. D.; Verdi, C.; Milot, R. L.; Eperon, G. E.; Pérez-Osorio, M. A.; Snaith, H. J.; Giustino, F.; Johnston, M. B.; Herz, L. M. Electron-phonon coupling in hybrid lead halide perovskites. *Nat. Comm.*, 2016, 7, 11755
- (43) Francisco-López, A.; Charles, B.; Weber, O. J.; Alonso, M. I.; Garriga, M.; Campoy-Quiles, M.; Weller, M. T.; Goñi, A. R. Equal Footing of Thermal Expansion and Electron-Phonon Interaction in the Temperature Dependence of Lead Halide Perovskite Band Gaps. *J. Phys. Chem. Lett.*, 2019, 10, 2971-2977
- (44) Herz, L. M. Charge-Carrier Dynamics in Organic-Inorganic Metal Halide Perovskites. *Annu. Rev. Phys. Chem.*, 2016, 67, 65-89
- (45) Kirchartz, T.; Krückemeier, L.; Unger, E. L. Research Update: Recombination and open-circuit voltage in lead-halide perovskites. *APL Mater.*, 2018, 6 (10), 100702
- (46) Milot, R. L.; Sutton, R. J.; Eperon, G. E.; Haghighirad, A. A.; Martinez Hardigree, J.; Miranda, L.; Snaith, H. J.; Johnston, M. B.; Herz, L. M. Charge-Carrier Dynamics in 2D Hybrid Metal-Halide Perovskites. *Nano Lett.*, 2016, 16(11), 7001-7007
- (47) Lee, J-W.; Kim, D-H.; Kim, H-S.; Seo, S-W.; Cho, S. M.; Park, N-P. Formamidinium and cesium hybridization for photo- and

1  
2  
3  
4  
5  
6  
7  
8  
9  
10  
11  
12  
13  
14  
15  
16  
17  
18  
19  
20  
21  
22  
23  
24  
25  
26  
27  
28  
29  
30  
31  
32  
33  
34  
35  
36  
37  
38  
39  
40  
41  
42  
43  
44  
45  
46  
47  
48  
49  
50  
51  
52  
53  
54  
55  
56  
57  
58  
59  
60

moisture-stable perovskite solar cell. Adv. En. Mater. 2015, 5,  
Charles, B.; Henry, P. F. Cs Mixed Cation Lead  
1501310  
Neutron and Muon Source, 2019, DOI:

(48) Weller, M. T.;  
Perovskites. STFC ISIS  
10.5286/ISIS.E.RB181  
0